Thermodynamic Study of Hydrogen Sulfide Corrosion of Mild Steel

Jing Ning,* Yougui Zheng,* David Young,* Bruce Brown,* and Srdjan Nešić[‡,*]

ABSTRACT

Expanding the basic knowledge required for improved understanding of hydrogen sulfide (H_2S) corrosion of mild steel is needed. When it comes to even the most basic chemical descriptors of aqueous H_2S systems such as H_2S solubility, water chemistry, polymorphism of iron sulfide, the formation or dissolution of iron sulfide scale, and its protectiveness, many open questions persist and more investigation is required. Inconsistencies in prevailing expressions for H_2S solubility constant (K_{H_2S}), the first dissociation constant ($K_{a,1}$), and the second dissociation constant ($K_{a,2}$) are reviewed here. By comparing with experimental data, the best prediction model for H_2S solubility and dissociation in an H_2S–H_2O system was identified. Occurrence of iron sulfide polymorphs was experimentally investigated and it was found that, in short-term exposures, mackinawite formed at 25°C, while greigite and pyrite were detected at 60°C. The solubility limits for these iron sulfides were determined. Simplified Pourbaix diagrams for the H_2S–H_2O–Fe system have been constructed with different meta-stable and stable iron sulfides (mackinawite, pyrrhotite, greigite, and pyrite) to predict the corrosion products in H_2S corrosion of mild steel.

KEY WORDS: dissociation constant, hydrogen sulfide, iron sulfide, polymorphous, Pourbaix diagram, solubility constant, solubility limit

PART 1—THERMODYNAMIC STUDY OF A H_2S–H_2O SYSTEM

Introduction

Hydrogen sulfide (H_2S) readily dissolves in water and partially dissociates. The reactions and the corresponding expressions with the solubility constants defining H_2S solubility and dissociation in an H_2S–H_2O system are shown as Reaction (1) through Equation (6).[1] Solubility is directly related to the partial pressure of H_2S (p_{H_2S}):

$$H_2S(g) \overset{K_{H_2S}}{\Leftrightarrow} H_2S(aq) \tag{1}$$
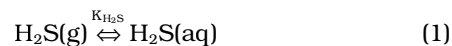
$$K_{H_2S} = [H_2S]/p_{H_2S} \tag{2}$$

The partial dissociations occur in two steps. The first dissociation (Reaction [3] and corresponding equilibrium Equation [4]) is followed by the second dissociation (Reaction [5] and corresponding equilibrium Equation [6]):

$$H_2S \overset{K_{a,1}}{\Leftrightarrow} H^+ + HS^- \tag{3}$$

$$K_{a,1} = [H^+][HS^-]/[H_2S] \tag{4}$$

$$HS^- \overset{K_{a,2}}{\Leftrightarrow} H^+ + S^{2-} \tag{5}$$

$$K_{a,2} = [H^+][S^{2-}]/[HS^-] \tag{6}$$

TABLE 1
Expressions for Solubility Constant K_{H_2S} from Multiple Sources

Equations	Values at 25°C	Sources
$K_{H_2S} = 10^{-[634.27+0.2709T_K-(0.11132\times10^{-3}T_K^2)-(16719/T_K)-(261.9\log T_K)]}$	0.097	Suleimenov[2]
$K_{H_2S} = 10^{-0.71742672-(0.012145427T_C)+(5.6659982\times10^{-5})T_C^2-(8.1902716\times10^{-8})T_C^3}$	0.103	IUPAC[3-4]
$K_{H_2S} = \exp[-41.0563+66.4005(\frac{100}{T_K})+15.1060\ln(\frac{T_K}{100})]$	0.102	Weiss[5]
$K_{H_2S} = 1/[10\times\exp(-3.3747+0.072437T_K-1.10765\times10^{-4}T_K^2-\frac{1549.159}{T_K}+0.144237\ln(T_K))-1]/0.018$	0.102	Carroll[6]
$K_{H_2S} = 10^{[82.7622+0.00831109T_K-(3898.56/T_K)-12.4914\ln(T_K)]}$	0.102	Roberts[7]

TABLE 2
Expressions for the First Dissociation Constant $K_{a,1}$ from Multiple Sources

Equations	Value at 25°C	Sources
$K_{a,1} = 10^{782.43945+0.361261T_K-(1.6722\times10^{-4})T_K^2-(20565.7315/T_K)-(142.741722\ln T_K)}$	1.052×10^{-7}	Suleimenov[8]
$K_{a,1} = 10^{-[15.345-0.045676T_K+(5.9666\times10^{-5})T_K^2]}$	9.319×10^{-8}	Kharaka[9]
$K_{a,1} = 10^{-[32.55+(1519.44/T_K)-(15.672\log T_K)-0.02722T_K]}$	1.041×10^{-7}	Millero[10]

TABLE 3
Values of the Second Dissociation Constant $K_{a,2}$ at 25°C

$K_{a,2}$ Value at 25°C	Sources
1.000×10^{-19}	Myers, 1986[11]
8.710×10^{-18}	Kharaka, 1989[9]
1.000×10^{-17}	Ellis, 1971[12]
1.000×10^{-16}	Licht, 1990[13]
1.000×10^{-15}	Skoog, 1982[14]
1.259×10^{-14}	Harris, 1995[15]
1.202×10^{-13}	Kolthoff, 1969[16]
1.000×10^{-12}	Su, 1997[17]

1. Sparge tube
2. Stir bar
3. pH probe
4. Temperature probe
5. Heater
6. Condenser
7. Syringe

FIGURE 1. *Experimental glass cell setup.*

Various expressions of the H_2S solubility constant (K_{H_2S}), the first dissociation constant ($K_{a,1}$), and the second dissociation constant ($K_{a,2}$) are used for calculating the water chemistries in a H_2S–H_2O system.[1] The prevalent expressions of the K_{H_2S}, $K_{a,1}$, and $K_{a,2}$ are listed in Tables 1 through 3, respectively. Therefore, verification of these expressions is needed to determine the best expressions for calculation of water chemistries in the H_2S–H_2O system.

EXPERIMENTAL PROCEDURES

Apparatus

Because of the inconsistencies of prevailing expressions for H_2S solubility and dissociation constants, experimental pH values were measured for verification purposes to check literature expressions and values for K_{H_2S}, $K_{a,1}$, and $K_{a,2}$. The experimental apparatus used for this investigation is shown in Figure 1.

Procedure

The glass cell was filled with 2 L of 1 wt% sodium chloride (NaCl) solution. Experiments were conducted after purging this solution with N_2 until saturation (typically a few hours). The H_2S and N_2 pre-mixed gas was then purged into the solution at a desired partial
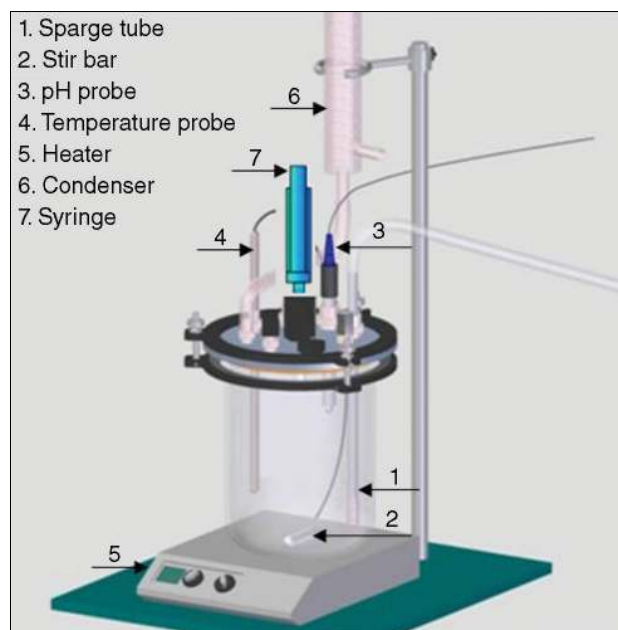
pressure, p_{H_2S}. After the pH value stabilized, another pre-mixed gas with higher p_{H_2S} was then purged into the solution, and the process was repeated. Experiments were performed for H_2S concentrations ranging from 40 ppm (p_{H_2S} = 0.0387 mbar at 25°C) to 8,000 ppm (p_{H_2S} = 7.75 mbar at 25°C) at 25°C, 60°C, and 80°C. The relationship between p_{H_2S} and measured pH value was obtained at 25°C, 60°C, and 80°C.

The resolution of the pH meter display was 0.01 pH unit and the overall accuracy of the pH meter was ±0.02 pH units. The pH meter/probe was checked by using pH buffer solutions (pH 4 and pH 7) at the desired temperature prior to every usage, to ensure that any pH drift was within ±0.01 pH unit. Otherwise recalibration was done at that temperature using the same pH buffer solutions (pH 4 and pH 7).
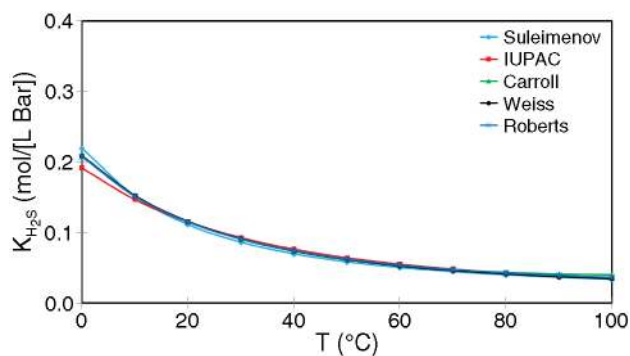
FIGURE 2. *Temperature dependency of the solubility constant K_{H_2S}.*

FIGURE 3. *Temperature dependency of first dissociation constant $K_{a,1}$.*

RESULTS AND DISCUSSION

Five prevalent equations used for K_{H_2S} calculation are shown in Table 1. All of these were used to find K_{H_2S} as a function of temperature. The K_{H_2S} change with temperature predicted by these five equations is shown in Figure 2, where all the five predicted curves are in good agreement. Arbitrarily, the expression of Suleimenov and Krupp[2] was selected for further use.

Three equations for predicting $K_{a,1}$ are shown in Table 2. Figure 3 shows $K_{a,1}$ dependency with temperature as predicted by these three equations. The curves predicted by Suleimenov and Seward[8] and Millero[10] are in agreement, but Kharaka, et al.,[9] show a different trend as temperature increases. The Suleimenov-Seward[8] expression was selected arbitrarily from the two expressions, which are in good agreement (Suleimenov and Seward[8] and Millero[10]), and the Kharaka, et al.,[9] expression was also selected to be used in two different versions of the pH prediction model, to find the more appropriate expression for this equilibrium constant.

The values of $K_{a,2}$ at 25°C were predicted by various models and are shown in Table 3. There is a large variation of $K_{a,2}$ values shown in Table 3 with the order of magnitude changing from 10^{-19} to 10^{-12}, resulting in a large uncertainty in sulfide ionic concentration. Consequently, using $K_{a,2}$ to calculate sulfide ionic concentration in the solution and to predict the solubility limit of iron sulfide should be avoided. However, any model used to predict pH is affected only slightly by this variation of $K_{a,2}$, due to the fact that most of the protons are formed by the first dissociation (Reaction [3]). The equation for $K_{a,2}$ proposed by Kharaka, et al.,[9] as shown in Equation (7), was used in the pH prediction model below:

$$K_{a,2} = 10^{-\left(23.93 - 0.030446 T_K + 2.4831 \times 10^{-5} T_K^2\right)} \qquad (7)$$

As discussed above, two pH value prediction models were obtained by combining these expressions for K_{H_2S}, $K_{a,1}$, and $K_{a,2}$, as shown in Table 4. Comparison of experimental pH with model predicted pH values at
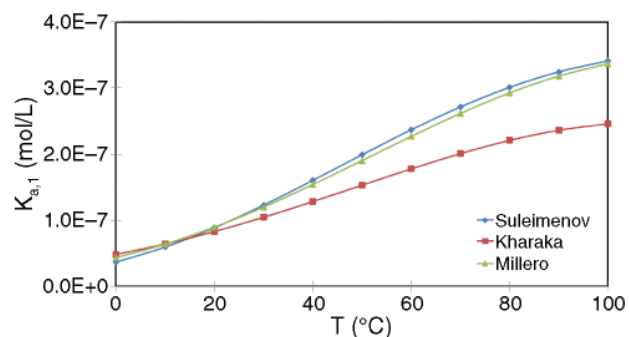
25°C, 60°C, and 80°C are shown in Figures 4 through 6, respectively. The comparison shows clearly that Model 1 is superior to Model 2.

CONCLUSIONS

Comparison of experimental pH value with predicted pH value based primarily on the correlations provided by Suleimenov, et al., (1994 and 1997) showed an excellent agreement; therefore, this model was selected to calculate water chemistry for a H_2S–H_2O system.

PART 2—THERMODYNAMIC STUDY OF A H_2S–H_2O–Fe^{2+} SYSTEM

Introduction

Polymorphs of iron sulfide are seen when it forms as a corrosion product in H_2S corrosion of mild steel, but the mechanisms related to the formation and transformation of various iron sulfides remain unclear. As a starting point, the solubility limits of various iron sulfides (K_{sp}) have been reviewed to gain a better understanding of the formation and dissolution of a given iron sulfide layer, and how this may be related to its protectiveness. The current research initially focuses on the solubility limit of mackinawite, as it initially forms as a corrosion product and, as a result of its meta-stability, can convert into other types of iron sulfide.[1] The solubility limit of mackinawite (K_{sp}) can be expressed at equilibrium conditions as shown by Reaction (8) and Equation (9):[1]

$$FeS + H^+ \overset{K_{sp,2}}{\Longleftrightarrow} Fe^{2+} + HS^- \qquad (8)$$

$$K_{sp,2} = \frac{[Fe^{2+}][HS^-]}{[H^+]} \qquad (9)$$

Several researchers have proposed solubility limit constants for mackinawite at 25°C; selected values for $K_{sp,2}$ from different literature sources are summarized in Table 5. Only Benning, et al.,[18] proposed an equa-

TABLE 4
Combinations of K_{H_2S}, $K_{a,1}$, and $K_{a,2}$ in pH Value Prediction Models

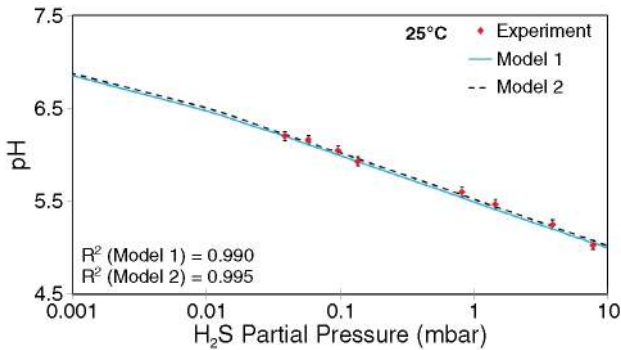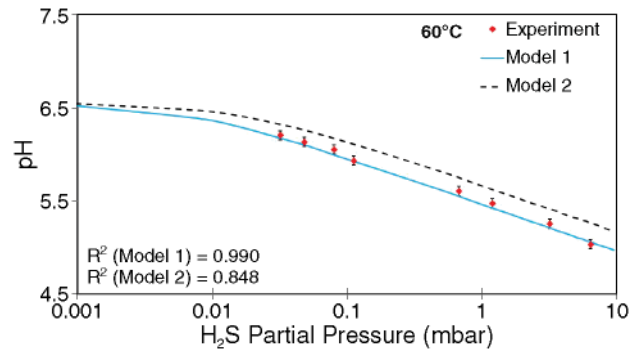| Models	K_{H_2S}	$K_{a,1}$	$K_{a,2}$
Model 1	Suleimenov, 1994[2]	Suleimenov, 1997[8]	Kharaka, 1989[9]
Model 2	Suleimenov, 1994[2]	Kharaka, 1989[9]	Kharaka, 1989[9]

FIGURE 4. *Comparison of experimental pH value with model predicted pH value at 25°C.*

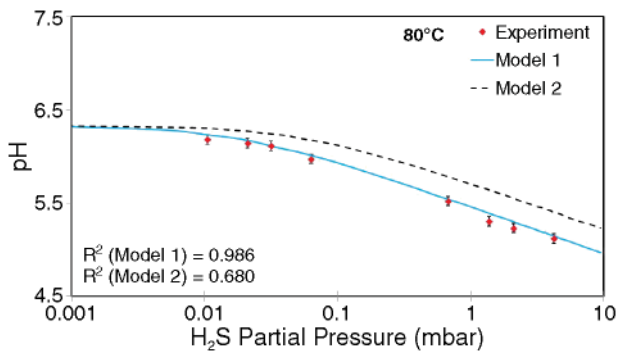**FIGURE 5.** *Comparison of experimental pH value with model predicted pH value at 60°C.*

FIGURE 6. *Comparison of experimental pH value with model predicted pH value at 80°C.*

TABLE 5
$pK_{sp,2}$ Values for Mackinawite from Literature at 25°C

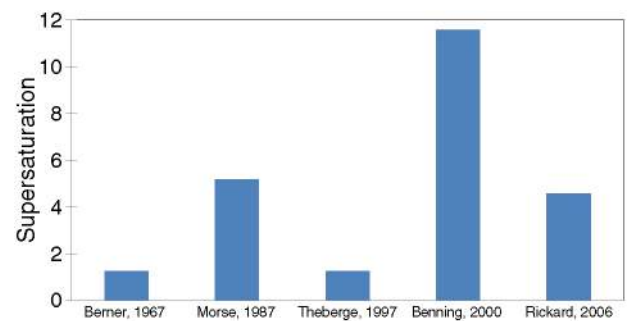| $pK_{sp,2}$ of Mackinawite at 25°C	Author
2.95	Berner, 1967[19]
3.55	Morse, 1987[20]
2.94	Theberge, 1997[21]
3.77	Benning, 2000[18]
3.5	Rickard, 2006[22]

FIGURE 7. *Calculated supersaturation values using $pK_{sp,2}$ values in Table 2 for the selected environment (25°C, p_{H_2S} = 0.97 mbar, $[Fe^{2+}]$ = 10 ppm, pH = 6).*

tion relating $K_{sp,2}$ for mackinawite to temperature as shown in Equation (10):

$$K_{sp,2} = 10^{\frac{2848.779}{T_K} - 6.347 + \log(K_{a,1,H_2S})} \qquad (10)$$

A specific environment was defined (25°C, p_{H_2S} = 0.97 mbar, $[Fe^{2+}]$ = 10 ppm, pH = 6) and saturation values were calculated using Equation (11) with the various $pK_{sp,2}$ values for mackinawite as shown in Table 5. Calculated supersaturation (SS) values for the given conditions are shown in Figure 7.

$$SS = \frac{\frac{[Fe^{2+}][HS^-]}{[H^+]}}{K_{sp,2}} \qquad (11)$$

Note the variation of supersaturation values observed from Figure 7, as a result of the differences in solubility product constants proposed by the various authors. According to Berner[19] and Theberge and Luther,[21] the solution was close to saturation and the driving force for mackinawite precipitation was small. However, according to Benning, et al.,[18] mackinawite supersaturation was high and precipitation would readily occur. Supersaturation based upon $pK_{sp,2}$ values from Rickard[22] and Morse, et al.,[20] lie somewhere in between. This indicates that further research is needed to confirm the $K_{sp,2}$ of mackinawite, as well as for other iron sulfides.

EXPERIMENTAL PROCEDURES

Apparatus

The experimental apparatus used in this part of the study is shown in Figure 1. A syringe was used to add a deoxygenated ferrous chloride solution into the glass cell or to take sample solution from the glass cell.

Methodology

A method based on pH variation was used to judge reaction equilibria during precipitation and dissolution. From the iron sulfide reaction given by Equation (8), the pH value should be stable when this reaction reaches equilibrium. In these experiments, it was considered to be the case when pH values varied by less than 0.01 units over a one hour time period. Dissolved iron concentration was measured spectrophotometrically, and the hydrogen ion concentration was determined from the pH value at equilibrium. The bisulfide ion concentration was predicted from the previously verified H_2S–H_2O thermodynamic prediction model for hydrogen sulfide solubility and dissociation. The $K_{sp,2}$ value was calculated by Equation (9) at equilibrium.

Procedure

In the experiments, nitrogen was purged into the 1 wt% NaCl electrolyte until pH stabilized, then the H_2S/N_2 pre-mixed gas was introduced into the glass cell until saturation was achieved. Deoxygenated ferrous chloride solution was then injected into the glass cell. Since no precipitation was typically observed, deoxygenated 1.0 M sodium hydroxide (NaOH) was injected to increase pH and induce precipitation. The experiment was then left unperturbed and its pH value monitored. Then, a deoxygenated 1.0 M hydrochloric acid (HCl) was gradually injected into the glass cell to facilitate dissolution of an existing precipitate. This process was repeated to obtain other equilibrium points during precipitation and dissolution of various iron sulfides. Samples of the solution were taken from the glass cell and a 0.45 μm syringe filter was used to separate the precipitate from the solution before measuring ferrous ion concentration of the solution spectrophotometrically. The separation process was performed by filtration in an oxygen-free environment using a glove box. Recovered solid precipitate was dried in a nitrogen environment before x-ray diffraction (XRD) analysis.

RESULTS AND DISCUSSION

Measured $pK_{sp,2}$ Values of Iron Sulfide Formed at 25°C

Three groups of experiments have been conducted to measure $pK_{sp,2}$ of formed iron sulfide:

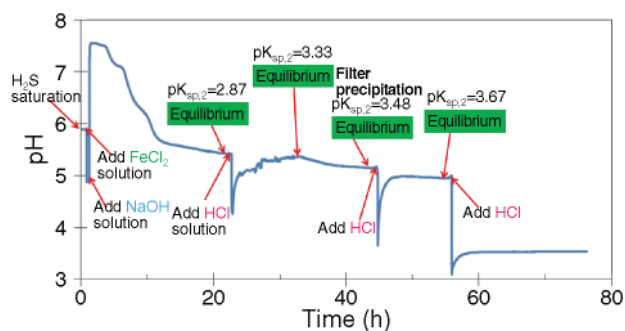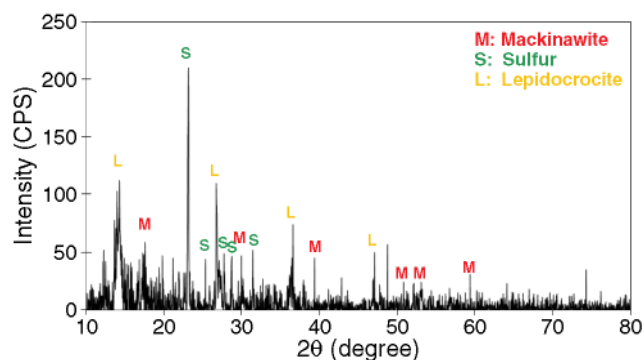**FIGURE 8.** *Measured $pK_{sp,2}$ at 200 ppm H_2S with adding HCl at 25°C.*

FIGURE 9. *XRD of precipitate ($pK_{sp,2}$ was 3.48).*

—at 200 ppm H_2S, adding HCl to facilitate dissolution of precipitate
—at 1,000 ppm H_2S, adding HCl
—at 200 ppm H_2S, without adding HCl

The results for the 200 ppm are shown in Figure 8. It was observed that measured $pK_{sp,2}$ values increased during the experiments starting at 2.87, then continued increasing to around 3.5. It was assumed that the $pK_{sp,2}$ value increased as a result of the iron sulfide type changing. Precipitate filtered from the glass cell when $pK_{sp,2}$ was 3.48 was sent for XRD to confirm this hypothesis.

Mackinawite, sulfur, and lepidocrocite were detected by XRD, as shown in Figure 9. The precipitate ($pK_{sp,2}$ was 3.48) was totally black when it was filtered and dried, but the surface color turned yellow/brown when it was taken out to do analysis. Craig[23] and Bourdoiseau, et al.,[24] also found the same: a mackinawite oxidation process, as given by Reaction (12). Mackinawite is readily oxidized to form lepidocrocite and sulfur when it is exposed to an oxygen-containing environment.

$$FeS + 3O_2 + 2H_2O \rightarrow 4FeO(OH) + 4S \qquad (12)$$

The result for 1,000 ppm H_2S also indicates that the $pK_{sp,2}$ value increased during the experiment, from 2.96 initially to 3.41. One more experiment for 200 ppm H_2S without adding HCl to dissolve the pre-
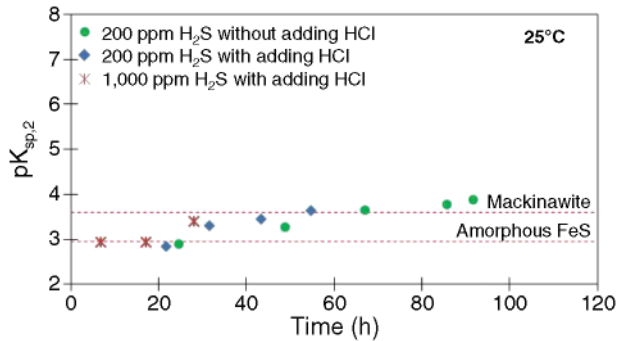
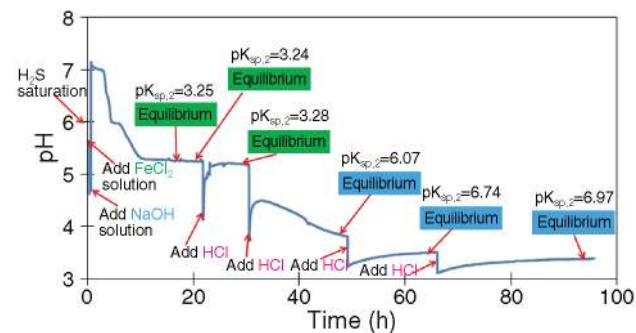**FIGURE 10.** *Summary of time dependence of $pK_{sp,2}$ at 25°C.*

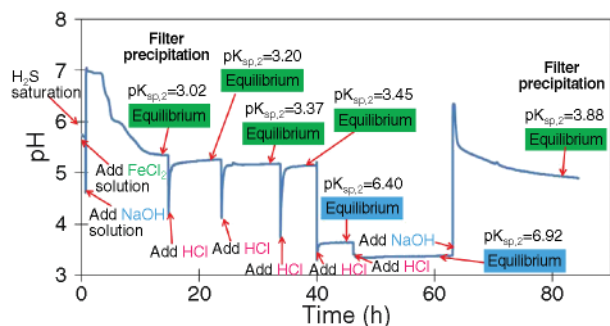**FIGURE 11.** *Measured $pK_{sp,2}$ at 200 ppm H_2S with adding HCl at 60°C.*

FIGURE 12. *Measured $pK_{sp,2}$ at 200 ppm H_2S with adding HCl/ NaOH at 60°C.*

cipitate was performed to check whether the increased $pK_{sp,2}$ value was related to time of exposure or pH value. The same phenomenon was observed and $pK_{sp,2}$ increased during experiments even though no HCl was added to adjust the pH. The data from these three experiments were combined and shown in Figure 10. Davison[25] reviewed current best estimates of $pK_{sp,2}$ at 25°C as shown in Table 6 and confirmed that amorphous iron sulfide formed during 1 h to 6 h of exposure time. The precipitate when $pK_{sp,2}$ was 3.48 at 200 ppm H_2S was confirmed to be mackinawite by XRD. The three experiments shown in Figure 10 were consistent with review by Davison,[25] suggesting that amorphous iron sulfide was formed initially ($pK_{sp,2}$ =

TABLE 6
Current Best Estimates of $pK_{sp,2}$ at 25°C from Literature[25]

Amorphous FeS	2.95±01
Mackinawite	3.6±0.2
Greigite	4.4±0.1
Pyrrhotite	5.1±0.15
Troilite	5.25±0.2
Pyrite	16.4±1.2

2.95±0.1) then converted to mackinawite ($pK_{sp,2}$ = 3.6±0.2).

Measured $pK_{sp,2}$ Values of Iron Sulfide Formed at 60°C

Experiments were also conducted at 60°C with 200 ppm H_2S and 1,000 ppm H_2S. The result of the 200 ppm H_2S experiments is shown in Figure 11 and the repeated result is shown in Figure 12. It is easy to observe that $pK_{sp,2}$ values can be divided into two groups: the "3 group" (with values clustered around $pK_{sp,2} \approx 3$ shown by green highlights) and the "6 group" (with values clustered around $pK_{sp,2} \approx 6$ and shown by blue highlights in Figures 11 and 12). It was assumed that the $pK_{sp,2}$ value difference was due to the iron sulfide type changing, but whether this change was truly related to the pH value or an artifact of the experimental duration and sequence was unclear. Deoxygenated sodium hydroxide solution was added to adjust pH values from 3.3 to 5.0, and the $pK_{sp,2}$ value decreased from 6.92 to 3.88 at the last point in Figure 12, which confirmed that the $pK_{sp,2}$ value change was a result of the pH value. Precipitate filtered from the glass cell when $pK_{sp,2}$ was measured to be 3.02 and 3.88 in Figure 12 and was then sent for analysis by XRD. Both greigite and pyrite were detected for these two samples, as shown in Figures 13 and 14, with greigite being dominant.

The results for 1,000 ppm H_2S are shown in Figure 15 and the repeated test is shown in Figure 16. It was also observed that the $pK_{sp,2}$ values differed between the "3 group" shown with green highlights and the "6 group" shown with blue highlights in Figures 15 and 16. The precipitate was filtered for analysis, taken when $pK_{sp,2}$ was 6.45 as shown in Figure 15 and taken when $pK_{sp,2}$ was 6.30 as shown in Figure 16. The XRD of the precipitate are shown in Figures 17 and 18, respectively. The XRD data with $pK_{sp,2}$ values of 6.45 and 6.30 showed that both precipitates were a mixture of greigite and pyrite, with the latter being dominant. Therefore, it is postulated that pyrite is dominant for $pK_{sp,2}$ value "6 group" precipitates.

Recalculation of $pK_{sp,2}$ Values of Greigite and Pyrite

Solubility reactions of greigite (Fe_3S_4) and pyrite (FeS_2) are written as Reaction (13) and Reaction (15) according to Berner,[19] Morse, et al.,[20] Davison,[25] and Rickard and Luther.[26]
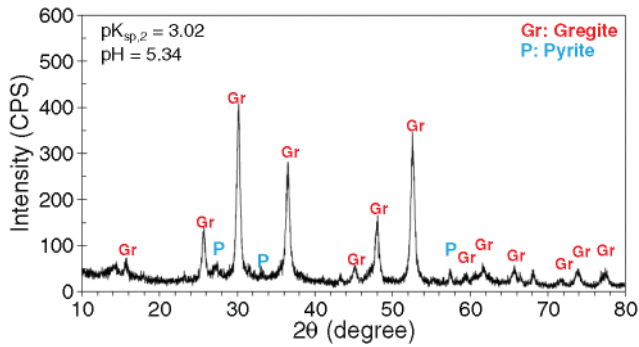
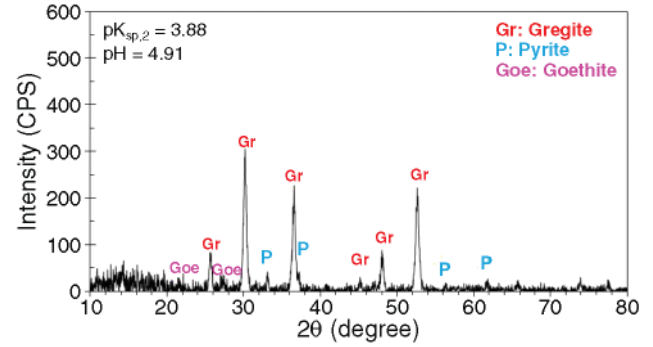**FIGURE 13.** *XRD of precipitate ($pK_{sp,2}$ was 3.02).*

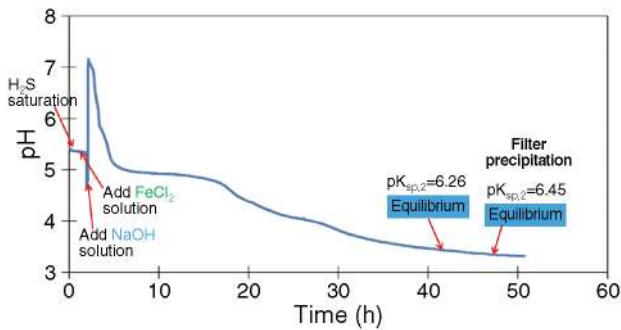**FIGURE 14.** *XRD of precipitate ($pK_{sp,2}$ was 3.88).*

FIGURE 15. *Measured $pK_{sp,2}$ at 1,000 ppm H_2S without adding HCl at 60°C.*
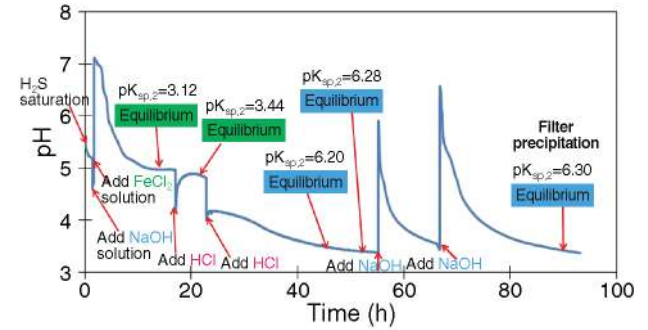

FIGURE 16. *Measured $pK_{sp,2}$ at 1,000 ppm H_2S with adding HCl/ NaOH at 60°C.*
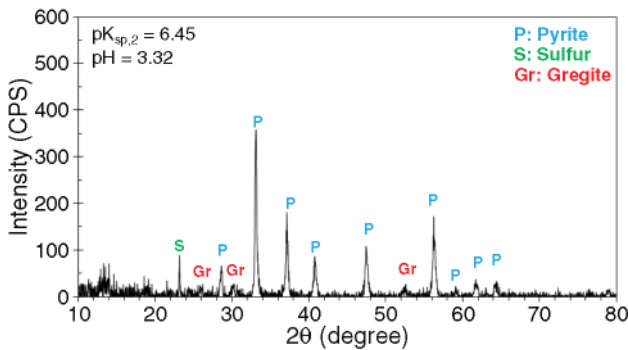

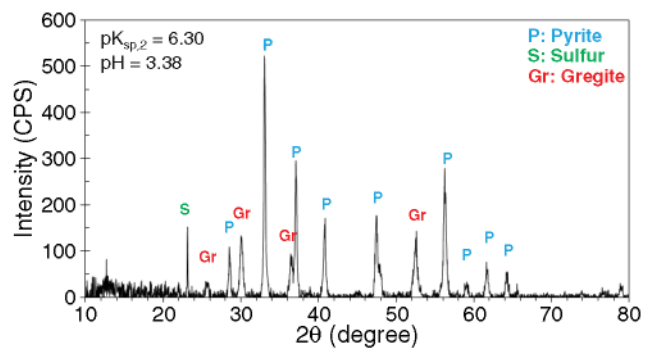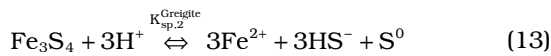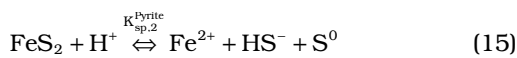
FIGURE 17. *XRD of precipitate ($pK_{sp,2}$ was 6.45).*

FIGURE 18. *XRD of precipitate ($pK_{sp,2}$ was 6.30).*

$$Fe_3S_4 + 3H^+ \overset{K_{sp,2}^{Greigite}}{\Leftrightarrow} 3Fe^{2+} + 3HS^- + S^0 \tag{13}$$

$$K_{sp,2}^{Greigite} = \left(\frac{[Fe^{2+}][HS^-]}{[H^+]} \right)^3 \tag{14}$$

$$FeS_2 + H^+ \overset{K_{sp,2}^{Pyrite}}{\Leftrightarrow} Fe^{2+} + HS^- + S^0 \tag{15}$$

$$K_{sp,2}^{Pyrite} = \frac{[Fe^{2+}][HS^-]}{[H^+]} \tag{16}$$

The $pK_{sp,2}$ values were recalculated as Equations (14) and (16) shown for greigite and pyrite, respectively. The recalculation of $pK_{sp,2}$ values were plotted

with the pH value shown in Figure 19. Two groups can be seen from Figure 19; pyrite formed around pH 3.5 and greigite formed around pH 5.0.

CONCLUSIONS

At 25°C, the measured $K_{sp,2}$ values were observed to increase with time, as a result of the iron sulfide type changing. It is believed that amorphous iron sulfide formed at the beginning then converted into mackinawite. Corresponding $pK_{sp,2}$ of mackinawite at 25°C was measured as 3.6±0.2. Polymorphs of iron sulfides (pyrite and greigite) were observed in the H_2S–H_2O–Fe^{2+} system at 60°C. For the investigated condition, greigite was dominant around pH 5 with
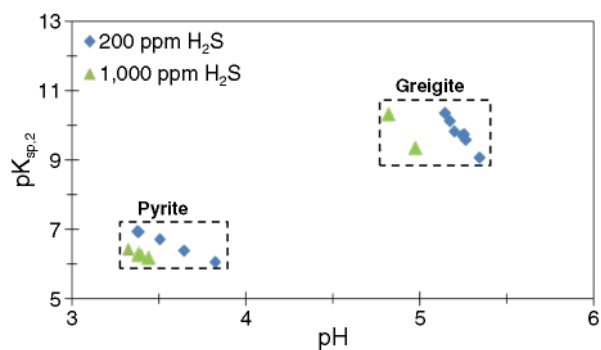
FIGURE 19. *Summary of pH-recalculated $pK_{sp,2}$ at 60°C.*

corresponding $pK_{sp,2}$ 9.8 ± 0.5, while pyrite was dominant around pH 3.5 with $pK_{sp,2}$ 6.5±0.5.

PART 3—POURBAIX DIAGRAMS FOR A H_2S–H_2O–Fe SYSTEM

Introduction

Polymorphous iron sulfides can form in H_2S corrosion including amorphous iron sulfide (FeS), mackinawite (FeS), cubic ferrous sulfide (FeS), troilite (FeS), pyrrhotites ($Fe_{1-x}S$), smythite ($Fe_{3+x}S_4$), greigite (Fe_3S_4), pyrite (FeS_2), and marcasite (FeS_2).[27-28] Some physicochemical properties of polymorphous iron sulfides are listed in Table 7.

Mackinawite, cubic ferrous sulfide, troilite, pyrrhotite, greigite, and pyrite have all been detected as corrosion products for mild steel in previously reported small- and large-scale laboratory tests.[29-33] It is broadly believed that different corrosion products have different effects on mild steel corrosion in H_2S environments due to their different physicochemical properties.[34-35] Development and verification of a thermodynamic prediction model for corrosion products seen in H_2S corrosion of mild steel is critical in an effort to better understand their effect on corrosion.

This will also be of key importance for the development of corrosion mitigation strategies in sour systems.

Amorphous Iron Sulfide (FeS)

Amorphous iron sulfide can only be detected by XRD as broadened low-intensity peaks, so usually it is assumed that it lacks any sort of long-range order (crystallinity). Kornicker[36] found that the physical properties of amorphous iron sulfide changed after drying, which might indicate that amorphous iron sulfide is a hydrate. Wolthers, et al.,[37] used low-angle x-ray powder diffraction (LAXRPD) to determine that "amorphous iron sulfide" is nanocrystalline mackinawite with an average particle size of 2.2±1.7 nm. Rickard and coworkers[38-39] concluded that "amorphous FeS" does not exist. They also stated that "amorphous iron sulfide," which first precipitates from bulk solution, is nanocrystalline mackinawite and confirmed that it is not hydrated by using nuclear magnetic resonance (NMR) spectroscopy and thermogravimetric analysis (TGA).

Mackinawite (FeS)

Mackinawite is widely considered to be the initial corrosion product in H_2S corrosion because of its rapid formation kinetics, and then converts into other iron sulfides depending on environmental conditions. The crystal structure of mackinawite consists of 2D layers, as shown in Figure 20(a). The composition of mackinawite is usually stated as iron-rich, $Fe_{1+x}S$ (x = 0 to 0.11). Berner[19] reported $Fe_{0.91}S$, Sweeney and Kaplan[40] found $Fe_{1.09-1.15}S$, Ward[41] reported $Fe_{0.995-1.023}S$, and Lennie and Vaughan[42] proposed $Fe_{0.99\pm0.02}S$. It was Rickard and Luther[26] who suggested that the reasons for previous researchers obtaining the composition of mackinawite as iron-rich, $Fe_{1+x}S$, are due to an analytical artifact relating to the presence of other metals in mineralogical samples. Rickard, et al.,[43] measured the composition of mackinawite as stoichiometric FeS.

TABLE 7
Polymorphous Iron Sulfides

| Name	Chemical Formula	Crystal Structure	Properties
Amorphous	FeS	Nano-crystalline	Unstable, converts into mackinawite quickly.
Mackinawite	FeS	Tetragonal, 2D layer	Metastable, the initial corrosion product.
Cubic FeS	FeS	Cubic	Very unstable, can transform into mackinawite, troilite, or pyrrhotite, never found naturally.
Troilite	FeS	Hexagonal	Stoichiometric end member of the $Fe_{1-x}S$ group (x = 0).
Pyrrhotite	$Fe_{1-x}S$ (x = 0 to 0.17)	Monoclinic Fe_7S_8 or hexagonal $Fe_{10}S_{11}$	Thermodynamically stable, the most abundant iron sulfide in the Earth.
Smythite	$Fe_{3+x}S_4$ (x = 0 to 0.3)	Trigonal-hexagonal	Metastable, related to the $Fe_{1-x}S$ group.
Greigite	Fe_3S_4	Cubic	Metastable $Fe^{2+}Fe^{3+}$ sulfide.
Pyrite	FeS_2	Cubic	Thermodynamically stable iron disulfide, the most abundant mineral on the Earth's surface
Marcasite	FeS_2	Orthorhombic	Metastable, common mineral in hydrothermal system and sedimentary rocks.
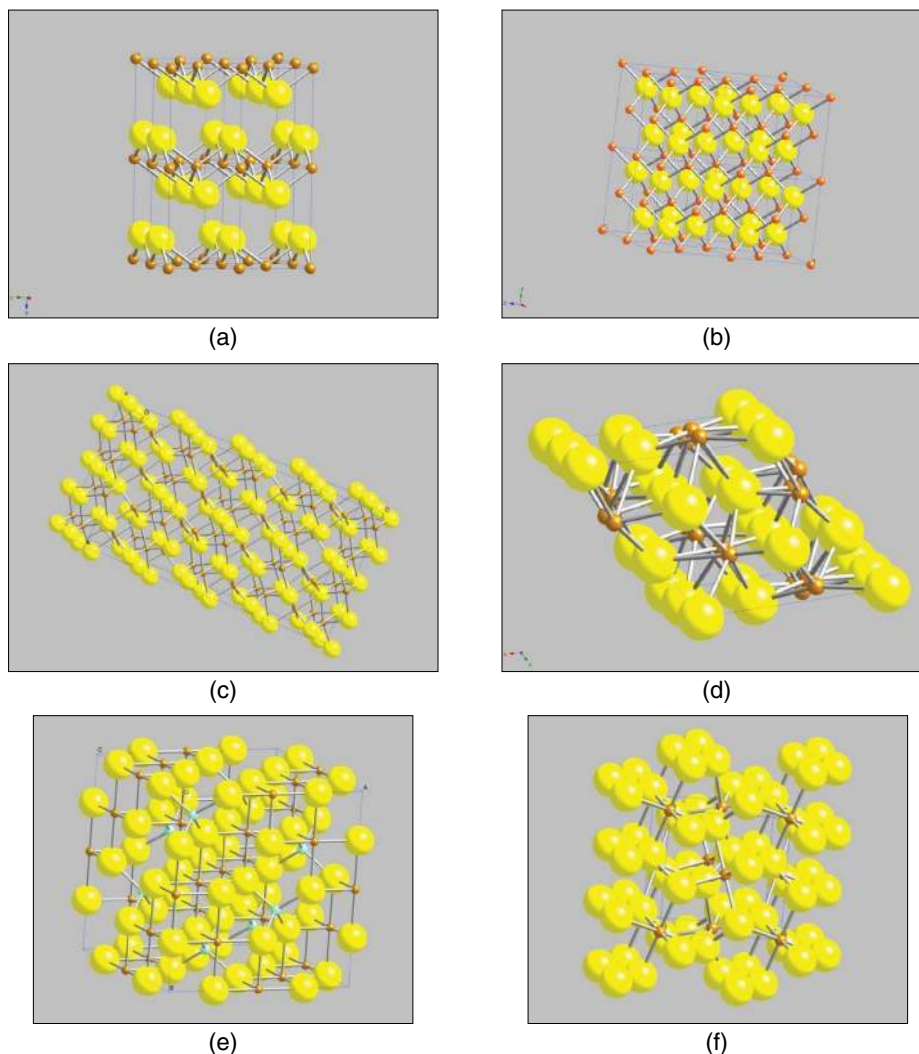
FIGURE 20. *Crystal structures of: (a) mackinawite; (b) cubic iron sulfide; (c) pyrrhotite; (d) troilite; (e) greigite; (f) pyrite generated by CrystalMaker[†].*

Cubic Iron Sulfide (FeS)

The crystal structure of cubic iron sulfide is illustrated in Figure 20(b). De Médicis[44] determined that cubic FeS did not form in the presence of oxygen or chlorides. Murowchik and Barnes[45] also discovered that cubic FeS can only crystallize at temperatures less than 92°C and at pH values between 2 and 6 in 4 h to 85 h, with its formation impeded by the presence of chlorides. Smith and Joosten[34] concluded that cubic iron sulfide is a transitional product that degrades into mackinawite, troilite, or pyrrhotite over several days, and that it is not a major constituent of any long-term corrosion product; it has only been observed in the laboratory, so it is not expected to be found in field conditions.

Cubic FeS has been detected in the so-called top-of-the-line corrosion (TLC),[32] where pure condensed water is seen. It can be excluded from the current study, which primarily focuses on the so-called bottom-of-the-line corrosion, that chlorides are normally present in the produced water.

Pyrrhotite (Fe$_{1-x}$S [x = 0 to 0.17]) and Troilite (FeS)

Pyrrhotite is actually a non-stoichiometric group of iron sulfides with formulae corresponding to Fe$_{1-x}$S (x = 0 to 0.17), where troilite is the stoichiometric end member of the pyrrhotite group when x = 0 (FeS). The crystal structures of pyrrhotite and troilite are shown in Figures 20(c) and (d). Pyrrhotite and troilite are thermodynamically stable; these two coexist below 150°C.[46] Troilite and pyrrhotite are differentiated only because the crystals that nucleate seem to initially grow differently at temperatures below 150°C. Troilite can be viewed as low-temperature and stoichiometric pyrrhotite. A variety of different pyrrhotites have been observed with different values of x resulting in changes in the unit cells of each.

[†] Trade name.

Smythite (Fe$_{3+x}$S$_4$[x = 0 to 0.3])

Smythite is the least studied iron sulfide and has not been reported as a corrosion product,[34] so it can be excluded from this study.

Greigite (Fe$_3$S$_4$)

The crystal structure of greigite is shown in Figure 20(e). Greigite is thermodynamically metastable; Lennie and Vaughan[42] noted that greigite is often present as an intermediary between the initial corrosion product mackinawite and the final product pyrite.

Pyrite (FeS$_2$)

Pyrite is the most abundant sulfide mineral in nature, also known as "fool's gold". The lattice crystal structure of pyrite is shown in Figure 20(f). Pyrite and pyrrhotite are the most stable iron sulfides, and considered to be the corrosion products seen in long exposures.

Marcasite (FeS$_2$)

Marcasite is compositionally identical to pyrite, but structurally different. Benning, et al.,[18] found the absence of marcasite under both reducing and oxidizing conditions in corrosion testing. Marcasite is not a typical corrosion product, and the publications related to marcasite are primarily in the geological literature, such as the work of Schoonen and Barnes[47] and Murowchick and Barnes.[45] There is no clear evidence that marcasite appears in corrosion environments, so marcasite is not taken into consideration here to be relevant in corrosion studies.

CONCLUSIONS

The polymorphous character of iron sulfides have been classified above primarily based on whether they were found in corrosion of mild steel in oil and gas systems. This was done to generate relatively simple Pourbaix diagrams dedicated to internal pipeline corrosion environments. The iron sulfides that have been taken into consideration for generating Pourbaix diagrams below are mackinawite, pyrrhotite, greigite, and pyrite.

CONSTRUCTION OF POURBAIX DIAGRAM FOR A H$_2$S–H$_2$O–Fe SYSTEM AT 25°C

A thermodynamic stability diagram (E vs. pH), also known as a Pourbaix diagram, is one of the most prominent contributions to corrosion science made by Pourbaix.[48-49] Pourbaix diagrams are used to map behavior of metal in aqueous solutions and thermodynamically stable corrosion products for practical purposes. Bouet and Brenet[50] have developed Pourbaix diagrams for H$_2$S–H$_2$O–Fe systems with iron sulfides FeS, FeS$_2$, and Fe$_2$S$_3$. Ueda[51] generated Pourbaix diagrams for a H$_2$O–CO$_2$/H$_2$S–Fe system with FeS and

FeS$_2$. Anderko and coworkers[52-53] referred to a commercial software package used to calculate and plot Pourbaix diagrams, including amorphous iron sulfide, mackinawite, greigite, marcasite, pyrite, and stoichiometric pyrrhotite. Discrepancies between Pourbaix diagrams representing the same species associated with sour corrosion from these authors are a result of variations in the sources of thermodynamic data, the different types of iron sulfides considered, and the diversity of reactions considered. Moreover, the unknown background details pertaining to commercial software packages used for the generation of Pourbaix diagrams makes it hard for corrosion engineers to understand and interpret the results they produce. Therefore, considering the relatively narrow corrosion focus in this study, development of Pourbaix diagrams for corrosion of mild steel in aqueous H$_2$S solutions is shown below in a stepwise fashion, accompanied by a complete account for all the assumptions, underlying thermodynamic data and reaction mechanisms.

As a starting point, Pourbaix diagrams for a H$_2$S–H$_2$O–Fe system were constructed at reference temperature (25°C) and constant H$_2$S partial pressure.

Thermodynamic Background

Corrosion is an electrochemical process that includes reduction and oxidation reactions. From the first and second laws of thermodynamics, one can write:

$$\Delta G + zFE = \Delta \tilde{G} \tag{17}$$

where ΔG represents the Gibbs energy change of a chemical reaction, zFE represents the electrical energy, and $\Delta \tilde{G}$ represents the total Gibbs energy change of an electrochemical reaction. At electrochemical equilibrium, $\Delta \tilde{G} = 0$, Equation (17) becomes:

$$\Delta G = -zFE_{rev} \tag{18}$$

where E_{rev} represents the reversible potential at equilibrium.

After transformation, the Nernst equation is obtained to calculate E_{rev} of an electrochemical reaction at equilibrium for any given set of conditions:

$$E_{rev} = E_{rev}^o - \frac{RT}{zF} \sum_{i=1}^{\kappa} \ln(c_i)^{n_i} \tag{19}$$

where E_{rev}^o represents the standard reversible potential that is defined at unit concentrations, reference temperature, and reference pressure. It can be computed from:

$$E_{rev}^o = -\Delta G_r^o / zF \tag{20}$$

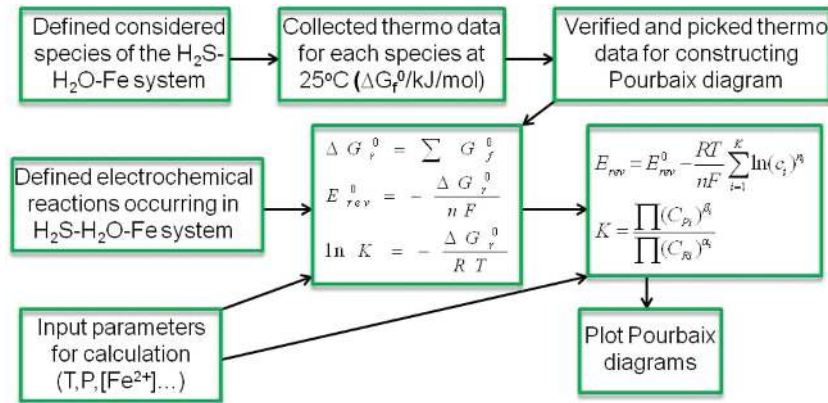where ΔG_r^o represents the Gibbs energy change of the electrochemical reaction.

FIGURE 21. *Process of generating Pourbaix diagrams.*

For example, the iron deposition/dissolution reaction is an electrochemical reaction shown by Equation (21). The Gibbs energy change of Reaction (21) is expressed in Equation (22).

$$Fe^{2+} + 2e^- \Leftrightarrow Fe \qquad (21)$$

$$\Delta G_r^o = G_{Fe}^0 - G_{Fe^{2+}}^0 - 2G_{e^-}^0 \qquad (22)$$

The standard reversible potential of Reaction (21), $E_{rev(Fe^{2+}/Fe)}^o$, is calculated by Equation (20), and then it is substituted into Equation (19) to calculate the reversible potential of the Reaction (21), $E_{rev(Fe^{2+}/Fe)}$.

$$E_{rev(Fe^{2+}/Fe)} = E_{rev(Fe^{2+}/Fe)}^o + \frac{RT}{2F}\ln(c_{Fe^{2+}}) \qquad (23)$$

For a pure chemical reaction, where there is no electron exchange in the reaction, the equilibrium condition can be written as:

$$\Delta G_r^o = -RT\sum_{i=1}^{k}\ln(c_i)^{n_i} \qquad (24)$$

The process of generating Pourbaix diagrams for a H_2S–H_2O–Fe system generally followed the steps shown in Figure 21.

The thermodynamic data for the considered species is listed in Table 8. The input parameters are shown in Table 9.

Pourbaix Diagram for a H_2O–Fe System at 25°C

To construct Pourbaix diagrams for a H_2S–H_2O–Fe system, the H_2O–Fe system was used as the starting point. All the equilibria for electrochemical and chemical reactions occurring in the H_2O–Fe system are listed in the second column in Table 10. The Nernst equation, Equation (19), is used for electrochemical reactions to calculate the reversible potential at equilibrium, and Equation (24) is used for chemical reactions to compute the equilibrium pH. The expressions

TABLE 8

Thermodynamic Data of the Considered Species of H_2S–H_2O–Fe System

Species	ΔG_f^0 (kJ/mol)	Source
H^+ (aq)	0	54
H_2S (g)	−33.329	55
H_2O (l)	−237.141	55
H_2 (aq)	17.74	54
O_2 (aq)	16.53	54
Fe (s)	0	55
Fe^{2+} (aq)	−91.5	54
Fe^{3+} (aq)	−17.24	54
Fe_2O_3 (s)	−743.523	55
Fe_3O_4 (s)	−1,017.438	55
$Fe(OH)_2$ (s)	−491.969	55
$Fe(OH)_3$ (s)	−705.467	55
FeS (mackinawite) (s)	−100.07	Calculated from Part II
Fe_3S_4 (greigite) (s)	−311.88	Recalculated from [19]
FeS (pyrrhotite) (s)	−101.95	56
FeS_2 (pyrite) (s)	−160.06	56

TABLE 9
Input Parameters

Temperature	25°C
P_{total}	1 bar
p_{H_2S}	0.0968 bar (10%)
$[Fe^{2+}]$	1.79×10^{-4} mol/L (10 ppm)
$[Fe^{3+}]$	1.0×10^{-6} mol/L
p_{H_2}	1 bar
p_{O_2}	1 bar

for equilibrium potential and pH are shown in the last column in Table 10. Equation (20) is used to calculate the standard reversible potential, using the information derived in Table 8 and Table 9. The Pourbaix diagram for the H_2O–Fe system at 25°C is created for arbitrary conditions similar to the test parameters assumed in this work and is shown in Figure 22.

Pourbaix Diagram with Only Mackinawite in a H_2S–H_2O–Fe System at 25°C

Mackinawite is "added first" into the Pourbaix diagram for the H_2O–Fe system, since it is the initial

TABLE 10
Equilibria of Electrochemical Reactions Occurring in the H_2O–Fe System

No.	Reaction	Equilibrium Potential or pH
H	$2H^+ + 2e^- \Leftrightarrow H_2$	$E_{rev(H^+/H_2)} = E^0_{rev(H^+/H_2)} - \frac{RT}{2F}\ln\frac{pH_2}{[H^+]^2}$
O	$O_2 + 4H^+ + 4e^- \Leftrightarrow 2H_2O$	$E_{rev(O_2/H_2O)} = E^0_{rev(O_2/H_2O)} - \frac{RT}{4F}\ln\frac{1}{pO_2 \cdot [H^+]^4}$
1.	$Fe^{2+} + 2e^- \Leftrightarrow Fe$	$E_{rev(Fe^{2+}/Fe)} = E^0_{rev(Fe^{2+}/Fe)} - \frac{RT}{2F}\ln\frac{1}{[Fe^{2+}]}$
2.	$Fe^{3+} + e^- \Leftrightarrow Fe^{2+}$	$E_{rev(Fe^{3+}/Fe^{2+})} = E^0_{rev(Fe^{3+}/Fe^{2+})} - \frac{RT}{F}\ln\frac{[Fe^{2+}]}{[Fe^{3+}]}$
3.	$Fe^{2+} + 2H_2O \Leftrightarrow Fe(OH)_2 + 2H^+$	$pH_{(Fe^{2+}/Fe(OH)_2)} = -0.5\log(K_{(Fe^{2+}/Fe(OH)_2)}[Fe^{2+}])$
4.	$Fe(OH)_2 + 2H^+ + 2e^- \Leftrightarrow Fe + 2H_2O$	$E_{rev(Fe(OH)_2/Fe)} = E^0_{rev(Fe^{3+}/Fe^{2+})} - \frac{RT}{2F}\ln\frac{1}{[H^+]^2}$
5.	$Fe_3O_4 + 2H_2O + 2H^+ + 2e^- \Leftrightarrow 3Fe(OH)_2$	$E_{rev(Fe_3O_4/Fe(OH)_2)} = E^0_{rev(Fe_3O_4/Fe(OH)_2)} - \frac{RT}{2F}\ln\frac{1}{[H^+]^2}$
6.	$6Fe_2O_3 + 4H^+ + 4e^- \Leftrightarrow 4Fe_3O_4 + 2H_2O$	$E_{rev(Fe_2O_3/Fe_3O_4)} = E^0_{rev(Fe_2O_3/Fe_3O_4)} - \frac{RT}{4F}\ln\frac{1}{[H^+]^4}$
7.	$Fe_3O_4 + 8H^+ + 2e^- \Leftrightarrow 3Fe^{2+} + 4H_2O$	$E_{rev(Fe_3O_4/Fe^{2+})} = E^0_{rev(Fe_3O_4/Fe^{2+})} - \frac{RT}{2F}\ln\frac{[Fe^{2+}]}{[H^+]^8}$
8.	$2Fe_2O_3 + 12H^+ + 4e^- \Leftrightarrow 4Fe^{2+} + 6H_2O$	$E_{rev(Fe_2O_3/Fe^{2+})} = E^0_{rev(Fe_2O_3/Fe^{2+})} - \frac{RT}{4F}\ln\frac{[Fe^{2+}]^4}{[H^+]^{12}}$
9.	$2Fe^{3+} + 3H_2O \Leftrightarrow Fe_2O_3 + 6H^+$	$pH_{(Fe^{3+}/Fe_2O_3)} = -\frac{1}{6}\log(K_{(Fe^{3+}/Fe_2O_3)}[Fe^{3+}]^2)$
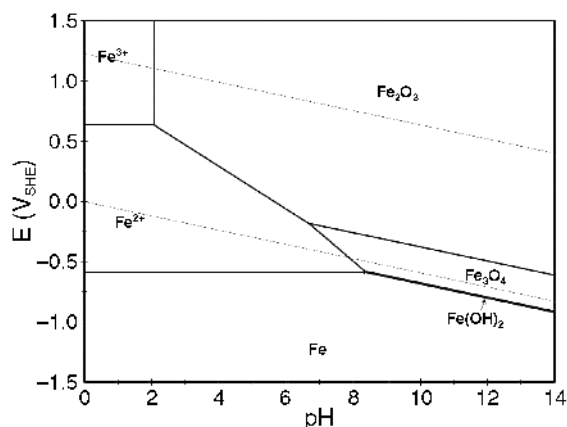
FIGURE 22. *Pourbaix diagram for H_2O–Fe system at 25°C.*

corrosion product in the presence of H_2S. The equilibria of reactions related to the formation of mackinawite (Reactions [10] through [14]) are listed in the second column in Table 11; the expressions for reversible potential and pH for each reaction are shown in the third column. When added into the H_2O–Fe system, and the graph, and after "cleaning up," the resulting diagram is shown in Figure 23(a). Mackinawite and ferric oxide (Fe_2O_3) are observed in Figure 23(a), while ferrous hydroxide ($Fe[OH]_2$) and magnetite (Fe_3O_4) have disappeared, being less stable than mackinawite.

Pourbaix Diagram with Mackinawite and Greigite in a H_2S–H_2O–Fe System at 25°C

The formation of greigite is considered next. The reactions ([15] through [19]) are taken into con-

sideration, as Table 11 shows, and the correlations between the reversible potential and pH for these reactions are also shown in Table 11. Figure 23(b) shows the Pourbaix diagram for which mackinawite and greigite have been accounted. Greigite is found in the higher potential range compared to mackinawite and significantly higher than would be typically seen in aqueous H_2S corrosion of mild steel.

Pourbaix Diagram with Mackinawite, Greigite, and Pyrrhotite in a H_2S–H_2O–Fe System at 25°C

The reactions related to the formation of pyrrhotite were incorporated next; reaction ([20] through [24]) details are shown in Table 11. The Pourbaix diagram with pyrrhotite added is shown in Figure 23(c). Note that mackinawite is no longer present since it is replaced by the more thermodynamically stable product pyrrhotite, which is the species to be expected in longer exposures under these conditions.

Pourbaix Diagram with Mackinawite, Greigite, Pyrrhotite, and Pyrite for H_2S–H_2O–Fe System at 25°C

The last of the dominant iron sulfides, pyrite, is added into the previous system. Reactions relating to the formation of pyrite (Reactions [25] through [31]) are given in Table 11. Figure 23(d) shows the Pourbaix diagram with all the four dominant iron sulfides considered. Only pyrrhotite and pyrite are present in Figure 23(d), indicating these two phases are the final and thermodynamically stable iron sulfide corrosion products, which are to be expected in long-term exposures. Given the typical potential and pH range

TABLE 11
Equilibria of Electrochemical Reactions Occurring in the $H_2S–H_2O–Fe$ System

No.	Reaction	Equilibrium Potential or pH
10.	$FeS_m + 2H^+ + 2e^- \Leftrightarrow Fe + H_2S(g)$	$E_{rev(FeS_m/Fe)} = E^0_{rev(FeS_m/Fe)} - \frac{RT}{2F}\ln\frac{pH_2S}{[H^+]^2}$
11.	$FeS_m + 2H^+ \Leftrightarrow Fe^{2+} + H_2S(g)$	$pH_{(FeS_m/Fe^{2+})} = -0.5\log\left(\frac{[Fe^{2+}]pH_2S}{K_{(FeS_m/Fe^{2+})}}\right)$
12.	$Fe_2O_3 + 2H_2S(g) + 2H^+ + 2e^- \Leftrightarrow 2FeS_m + 3H_2O$	$E_{rev(Fe_2O_3/FeS_m)} = E^0_{rev(Fe_2O_3/FeS_m)} - \frac{RT}{2F}\ln\frac{1}{pH_2S^2 \cdot [H^+]^2}$
13.	$Fe_3O_4 + 3H_2S(g) + 2H^+ + 2e^- \Leftrightarrow 3FeS_m + 4H_2O$	$E_{rev(Fe_3O_4/FeS_m)} = E^0_{rev(Fe_3O_4/FeS_m)} - \frac{RT}{2F}\ln\frac{1}{pH_2S^3 \cdot [H^+]^2}$
14.	$Fe(OH)_2 + H_2S(g) \Leftrightarrow FeS_m + 2H_2O$	$K_{(Fe(OH)_2/FeS_m)} = \frac{1}{pH_2S}$
15.	$Fe_3S_4 + 8H^+ + 8e^- \Leftrightarrow 3Fe + 4H_2S(g)$	$E_{rev(Fe_3S_4/Fe)} = E^0_{rev(Fe_3S_4/Fe)} - \frac{RT}{8F}\ln\frac{pH_2S^4}{[H^+]^8}$
16.	$Fe_3S_4 + 8H^+ + 2e^- \Leftrightarrow 3Fe^{2+} + 4H_2S(g)$	$E_{rev(Fe_3S_4/Fe^{2+})} = E^0_{rev(Fe_3S_4/Fe^{2+})} - \frac{RT}{2F}\ln\frac{[Fe^{2+}]^3 pH_2S^4}{[H^+]^8}$
17.	$3Fe^{3+} + 4H_2S(g) + e^- \Leftrightarrow Fe_3S_4 + 8H^+$	$E_{rev(Fe_2O_3/Fe_3S_4)} = E^0_{rev(Fe_2O_3/Fe_3S_4)} - \frac{RT}{2F}\ln\frac{1}{[H^+]^2 pH_2S^8}$
18.	$3Fe_2O_3 + 8H_2S(g) + 2H^+ + 2e^- \Leftrightarrow 2Fe_3S_4 + 9H_2O$	$E_{rev(Fe_2O_3/Fe_3S_4)} = E^0_{rev(Fe_2O_3/Fe_3S_4)} - \frac{RT}{2F}\ln\frac{1}{[H^+]^2 pH_2S^8}$
19.	$Fe_3S_4 + 2H^+ + 2e^- \Leftrightarrow 3FeS_m + H_2S(g)$	$E_{rev(Fe_3S_4/FeS_m)} = E^0_{rev(Fe_3S_4/FeS_m)} - \frac{RT}{2F}\ln\frac{pH_2S}{[H^+]^2}$
20.	$FeS_p + 2H^+ + 2e^- \Leftrightarrow Fe + H_2S(g)$	$E_{rev(FeS_{pyrrhotite}/Fe)} = E^0_{rev(FeS_{pyrrhotite}/Fe)} - \frac{RT}{2F}\ln\frac{pH_2S}{[H^+]^2}$
21.	$FeS_p + 2H^+ \Leftrightarrow Fe^{2+} + H_2S(g)$	$pH_{(FeS_{pyrrhotite}/Fe^{2+})} = \log\left(\frac{pH_2S \cdot [Fe^{2+}]}{K_{(FeS_{pyrrhotite}/Fe^{2+})}}\right)^{-\frac{1}{2}}$
22.	$Fe_2O_3 + 2H_2S(g) + 2H^+ + 2e^- \Leftrightarrow 2FeS_p + 3H_2O$	$E_{rev(Fe_2O_3/FeS_{pyrrhotite})} = E^0_{rev(Fe_2O_3/FeS_{pyrrhotite})} - \frac{RT}{2F}\ln\frac{1}{pH_2S^2 \cdot [H^+]^2}$
23.	$Fe_3S_4 + 2H^+ + 2e^- \Leftrightarrow 3FeS_p + H_2S(g)$	$E_{rev(Fe_3S_4/FeS_{pyrrhotite})} = E^0_{rev(Fe_2O_3/FeS_{pyrrhotite})} - \frac{RT}{2F}\ln\frac{pH_2S}{[H^+]^2}$
24.	$FeS_{Pyrrhotite} \Leftrightarrow FeS_{Mackinawite}$	$K_{(FeS_p/FeS_m)} = 1$
25.	$FeS_2 + 4H^+ + 2e^- \Leftrightarrow Fe^{2+} + 2H_2S(g)$	$E_{rev(FeS2pyrite/Fe^{2+})} = E^0_{rev(FeS2pyrite/Fe^{2+})} - \frac{RT}{2F}\ln\frac{[Fe^{2+}] \cdot pH_2S^2}{[H^+]^4}$
26.	$FeS_2 + 4H^+ + 4e^- \Leftrightarrow Fe + 2H_2S(g)$	$E_{rev(FeS2pyrite/Fe)} = E^0_{rev(FeS2pyrite/Fe)} - \frac{RT}{4F}\ln\frac{pH_2S^2}{[H^+]^4}$
27.	$2FeS_2 + 3H_2O + 2H^+ + 2e^- \Leftrightarrow Fe_2O_3 + 4H_2S(g)$	$E_{rev(FeS2pyrite/Fe_2O_3)} = E^0_{rev(FeS2pyrite/Fe_2O_3)} - \frac{RT}{2F}\ln\frac{pH_2S^4}{[H^+]^2}$
28.	$FeS_2 + 2H^+ + 2e^- \Leftrightarrow FeS_{Mackinawite} + H_2S(g)$	$E_{rev(FeS2pyrite/FeS_m)} = E^0_{rev(FeS2pyrite/FeS_m)} - \frac{RT}{2F}\ln\frac{pH_2S}{[H^+]^2}$
29.	$FeS_2 + 2H^+ + 2e^- \Leftrightarrow FeS_{Pyrrhotite} + H_2S(g)$	$E_{rev(FeS2pyrite/FeS_{pyrrhotite})} = E^0_{rev(FeS2pyrite/FeS_{pyrrhotite})} - \frac{RT}{2F}\ln\frac{pH_2S}{[H^+]^2}$
30.	$FeS_2 + 4H^+ + e^- \Leftrightarrow Fe^{3+} + 2H_2S(g)$	$E_{rev(FeS2pyrite/Fe^{3+})} = E^0_{rev(FeS2pyrite/Fe^{3+})} - \frac{RT}{F}\ln\frac{[Fe^{3+}] \cdot pH_2S^2}{[H^+]^4}$
31.	$3FeS_2 + 4H^+ + 4e^- \Leftrightarrow Fe_3S_4 + 2H_2S(g)$	$E_{rev(FeS2pyrite/FeS_{greigite})} = E^0_{rev(FeS2pyrite/FeS_{greigite})} - \frac{RT}{4F}\ln\frac{pH_2S^2}{[H^+]^4}$

encountered during internal corrosion of mild steel in aqueous H_2S solutions, pyrrhotite should be the main species expected in longer term exposures.

CONCLUSIONS

The key polymorphous iron sulfides relevant for corrosion of mild steel in oil and gas systems have been identified to be mackinawite (FeS), greigite (Fe_3S_4), pyrrhotite ($Fe_{1-x}S$, x = 0 to 0.17), and pyrite (FeS_2). The Pourbaix diagrams of the $H_2S–H_2O–Fe$ system at 25°C were constructed, indicating that under typical conditions seen during internal corrosion of mild steel in aqueous H_2S-containing solutions (poten-

tial and pH range) mackinawite should be expected in shorter exposures while pyrrhotite should be the key corrosion product seen in longer exposures. Because of the fast kinetics, mackinawite should be the most common species seen in short exposures. Greigite and pyrite are more likely to form at higher pH and higher potentials, more typical for oxygenated solutions.
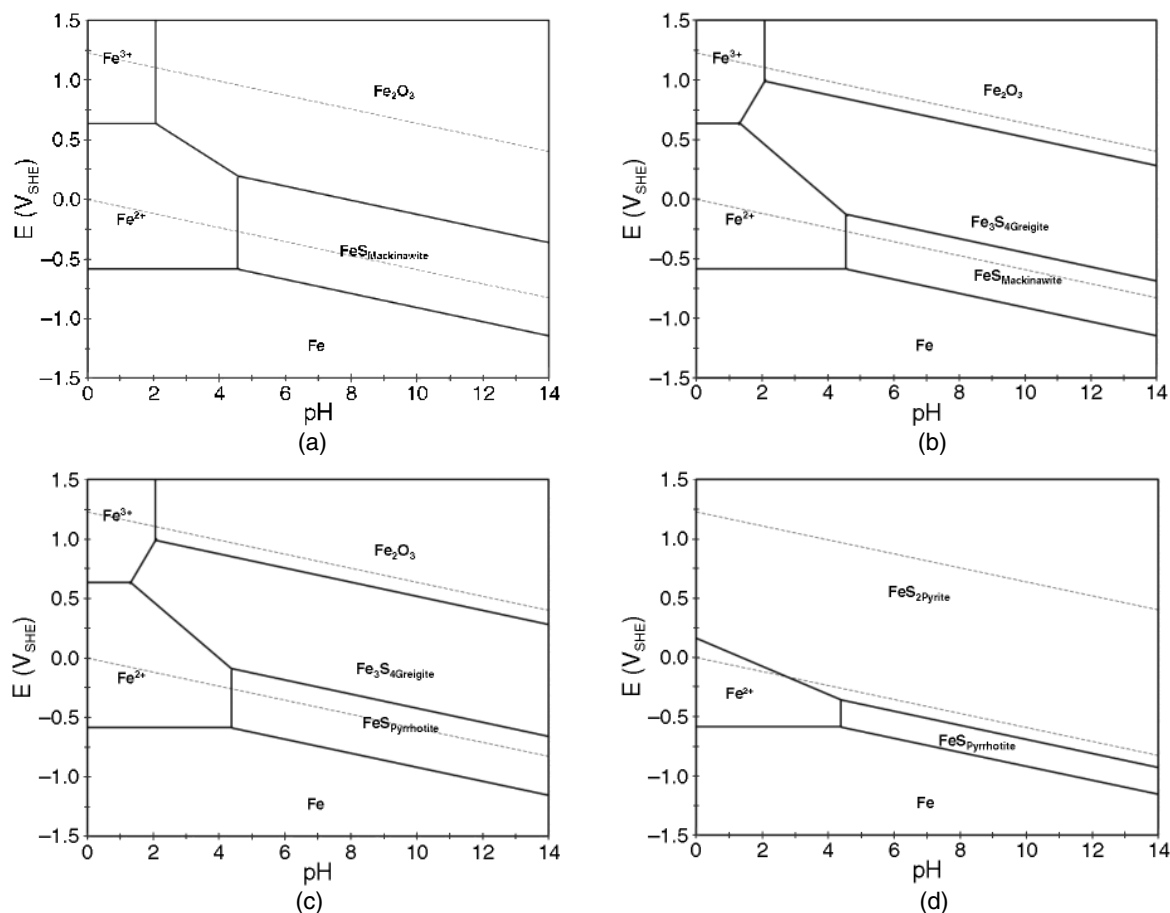
ACKNOWLEDGMENTS

FIGURE 23. *Pourbaix diagram for H₂S–H₂O–Fe system with (a) mackinawite; (b) mackinawite/greigite; (c) mackinawite/ greigite/pyrrhotite; (d) mackinawite/greigite/pyrrhotite/pyrite.*

REFERENCES

1. W. Sun, S. Nešić, D. Young, R. Woolam, *Ind. Eng. Chem. Res.* 47 (2008): p. 1738.
2. O.M. Suleimenov, R.E. Krupp, *Geochim. Cosmochim. Ac.* 58, 11 (1994): p. 2433-2444.
3. M. Nordsveen, S. Nešić, R. Nyborg, A. Stangeland, *Corrosion* 59, 5 (2003): p. 443-457.
4. E. Hogfeldt, *Stability Constants of Metal-Ion Complexes, Part A: Inorganic Ligands* (Oxford, U.K.: Pergamon Press, 1982).
5. R.F. Weiss, *Deep-Sea Res.* 17 (1970): p. 721-735.
6. J. Carroll, A.E. Mather, *Geochim. Cosmochim. Ac.* 53 (1989): p. 1163-1170.
7. B.E. Roberts, P.R. Tremaine, *Can. J. Chem. Eng.* 63 (1985): p. 294-300.
8. O.M. Suleimenov, T.M. Seward, *Geochim. Cosmochim. Ac.* 61, 24 (1997): p. 5187-5198.
9. Y.K. Kharaka, E.H. Perkins, W.D. Counter, J.D. Debral, C.H. Bamford, *Solmineq 88: A Computer Program for Geochemical Modeling of Water Rock Interactions* (Menlo Park, CA: Alberta Research Council, 1989).
10. F.J. Millero, *Mar. Chem.* 18 (1986): p. 121-147.
11. R.J. Myers, *J. Chem. Educ.* 63 (1986): p. 687-690.
12. A.J. Ellis, W. Giggenbach, *Geochim. Cosmochim. Acta* 35 (1971): p. 247-260.
13. S. Licht, F. Forouzan, K. Longo, *Anal. Chem.* 62 (1990): p. 1356-1360.
14. D.A. Skoog, D.M. West, *Fundamental of Analytical Chemistry*, 4th ed. (Philadelphia, PA: W.B. Saunders Co., 1982).
15. D.C. Harris, *Quantitative Chemical Analysis*, 4th ed. (New York: W.H. Freeman, 1995).
16. I.M. Kolthoff, E.B. Sandell, E.J. Meehan, S. Bruckenstein, *Quantitative Chemical Analysis*, 4th ed. (London, U.K.: Macmillan, 1969).
17. Y.S. Su, K.L. Cheng, Y.C. Jean, *Talanta* 44 (1997): p. 1757-1763.
18. L.G. Benning, R.T. Wilkin, H.L. Barnes, *Chem. Geol.* 167 (2000): p. 25-51.
19. R.A. Berner, *Am. J. Sci.* 265 (1967): p. 773-785.
20. J.W. Morse, F.J. Millero, J.C. Cornwell, D. Rickard, *Earth Sci. Rev.* 24 (1987): p. 1-42.
21. S. Theberge, G.W. Luther, *Aquat. Geochem.* 3 (1997): p. 191-211.
22. D. Rickard, *Geochim. Cosmochim. Acta* 70 (2006): p. 5779-5789.
23. D.B. Craig, *Corrosion* 35 (1979): p. 136-138.
24. J.A. Bourdoiseau, M. Jeannin, R. Sabot, C. Remazeilles, Ph. Refait, *Corros. Sci.* 50 (2008): p. 3247-3255.
25. W. Davison, *Aquat. Sci.* 53 (1991): p. 309-329.
26. D. Rickard, G.W. Luther, *Chem. Rev.* 107 (2007): p. 514-562.
27. P. Taylor, *Am. Mineral.* 65 (1980): p. 1026-1030.
28. J.S. Smith, J.D.A. Miller, *Br. Corros. J.* 10 (1975): p. 136-143.
29. S.N. Smith, B. Brown, W. Sun, "Corrosion At Higher H₂S Concentrations and Moderate Temperatures," CORROSION 2011, paper no. 11081 (Houston, TX: NACE, 2011).
30. W. Sun, "Kinetics of Iron Carbonate and Iron Sulfide Scale Formation in Carbon Dioxide/Hydrogen Sulfide Corrosion" (Ph.D. diss., Ohio University, 2006).

31. K. Lee, "A Mechanistic Modeling of CO_2 Corrosion of Mild Steel in the Presence of H_2S" (Ph.D. diss., Ohio University, 2004).
32. M. Singer, A. Camacho, B. Brown, S. Nešić, "Sour Top of the Line Corrosion in the Presence of Acetic Acid" CORROSION 2010, paper no. 10100 (Houston, TX: NACE, 2010).
33. M. Singer, S. Nešić, J.N. Al-Khamis, "Corrosion Assessment in Karan Gas Field Development" CORROSION 2012, paper no. 1411 (Houston, TX: NACE, 2012).
34. S.N. Smith, M. Joosten, "Corrosion of Carbon Steel by H_2S in CO_2 Containing Oilfield Environments," CORROSION/2006, paper no. 06115 (Houston, TX: NACE, 2006).
35. S.N. Smith, "A Proposed Mechanism for Corrosion in Slightly Sour Oil and Gas Production," 12th Int. Corros. Cong., paper no. 385, held Sept. 19-24 (Houston, TX: Int. Corrosion Congress, 1993).
36. W.A. Kornicker, "Interactions of Divalent Cations with Pyrite and Mackinawite in Seawater and NaCl Solutions" (Ph.D. diss., Texas A&M University, 1988).
37. M. Wolthers, S.J. Van der Gaast, D. Rickard, *Am. Mineral.* 88 (2003): p. 2007-2015.
38. D. Rickard, A. Griffith, A. Oldroyd, I.B. Butler, E. Lopez-Capel, D.A.C. Manning, D.C. Apperley, *Chem. Geol.* 235 (2006): p. 286-298.
39. J.W. Morse, D. Rickard, *Environ. Sci. Technol.* (2004): p. 131-136.
40. R.E. Sweeney, I.R. Kaplan, *Econ. Geol.* 68 (1973): p. 618-634.
41. J.C. Ward, *Rev. Pure Appl. Chem.* 20 (1970): p. 175-206.
42. A.R. Lennie, D.J. Vaughan, "Spectroscopic Studies of Iron Sulfide Formation and Phase Relations at Low Temperatures," in *Mineral Spectroscopy: A Tribute to Roger G. Burns*, eds. M. D. Dyar, C. McCammon, M.W. Schaefer (Houston, TX: The Geochemical Society, 1996).
43. D. Rickard, A. Griffith, A. Oldroyd, I.B. Butler, E. Lopez-Capel, D.A.C. Manning, D.C. Apperley, *Chem. Geol.* 235 (2006): p. 286-298.
44. R. de Médicis, *Science* 170 (1970): p. 1191-1192.
45. B.J. Murowchick, H.L. Barnes, *Am. Mineral.* 71 (1986): p. 1243-1246.
46. R.G. Arnold, *Econ. Geol.* 64 (1969): p. 405-419.
47. M. Schoonen, H.L. Barnes, *Geochim. Cosmochim. Ac.* 55 (1991): p. 1505-1514.
48. M. Pourbaix, *Atlas of Electrochemical Equilibria in Aqueous Solutions*, trans. J.A. Franklin (Houston, TX: NACE, 1974).
49. M. Pourbaix, *Lectures on Electrochemical Corrosion*, trans. J.A.S. Green, trans. ed. R.W. Staehle (New York, NY: Plenum Press, 1973).
50. J. Bouet, J.P. Brenet, *Corros. Sci.* 3 (1963): p. 51-63.
51. M. Ueda, *Corros. Eng.* 44, 3 (1995): p. 159-174.
52. A. Anderko, P.J. Shuler, *Comput. Geosci.* 23, 6 (1997): p. 647-658.
53. A. Anderko, S.J. Sanders, R.D. Young, *Corros. Sci.* 53, 1 (1997): p. 43-53.
54. E.H. Oelkers, H.C. Helgeson, E.L. Shock, D.A. Sverjensky, J.W. Johnson, V.A. Pokrovskii, *J. Phys. Chem. Ref. Data* 24, 4 (1995): p. 1401-1560.
55. M.W. Chase, J.R. Downey, *J. Phys. Chem. Ref. Data,* Monograph no. 9 (1998).
56. M.W. Chase, C.A. Davies, J.R. Downey, D.J. Fruip, R.A. Madonald, A.N. Syverud, *J. Phys. Chem. Ref. Data* 14, 1 (1985).